

Robust Piezoelectricity with Spontaneous Polarization in Monolayer Tellurene and Multilayer Tellurium Film at Room Temperature for Reliable Memory

Gaofeng Rao, Hui Fang, Ting Zhou, Chunlin Zhao, Nianze Shang, Jianwen Huang,*
Yuqing Liu, Xinchuan Du, Peng Li, Xian Jian, Liang Ma, Jinlan Wang, Kaihui Liu,
Jiagang Wu, Xianfu Wang,* and Jie Xiong*

Robust neuromorphic computing in the Big Data era calls for long-term stable crossbar-array memory cells; however, the elemental segregation in the switch unit and memory unit that inevitably occurs upon cycling breaks the compositional and structural stability, making the whole memory cell a failure. Searching for a novel material without segregation that can be used for both switch and memory units is the major concern to fabricate robust and reliable nonvolatile cross-array memory cells. Tellurium (Te) is found recently to be the only peculiar material without segregation for switching, but the memory function has not been demonstrated yet. Herein, apparent piezoelectricity is experimentally confirmed with spontaneous polarization behaviors in elementary 2D Te, even in monolayer tellurene (0.4 nm), due to the highly oriented polarization of the molecular structure and the non-centrosymmetric lattice structure. A large memory window of 7000, a low working voltage of 2 V, and high on switching current up to $36.6 \mu\text{A} \mu\text{m}^{-1}$ are achieved in the as-fabricated Te-based memory device, revealing the great promise of Te for both switching and memory units in one cell without segregation. The piezoelectric Te with spontaneous polarization provides a platform to build robust, reliable, and high-density logic-in-memory chips in neuromorphic computing.

inspired from the human brain,^[1] owns attractive features including highly parallel operation,^[2,3] inherent scalability,^[4] and extremely low power consumption^[5–7] compared with conventional Von Neumann architecture,^[8,9] exhibiting great expectation in the field of intelligence and machine learning including autonomous systems, robotics, artificial intelligence accelerators, remote sensing, etc.,^[10–13] The iterative learning process and continuously increased analogue weight updates in long-term neuromorphic computing urgently require highly reliable hardware, as the analogue weight will be changed causing the decreased system accuracy once the hardware is unreliable.^[14–16] As one of the most important and frequently-used structure for the basic reliable hardware of neuromorphic computing, the cross-array memory cell, composed of one switch unit and one memory unit, operates the calculation and data storage synergistically.^[1,17–19] Consequently, the cycling stability and endurance of the memory cell are major concern for highly-stable neuro-


morphic computer. However, the elemental segregation in the various materials used for switch unit and memory unit inevitably occurs upon cycling, which challenges the compositional and structural stability, making the memory cell a failure.^[20–22]

1. Introduction

Neuromorphic computing, a new architecture that carries out both processing and memory in neurons and synapses

G. F. Rao, T. Zhou, J. W. Huang, Y. Q. Liu, X. C. Du, P. Li, X. Jian,
X. F. Wang, J. Xiong
State Key Laboratory of Electronic Thin Film and Integrated Devices
University of Electronic Science and Technology of China
Chengdu 611731, China
E-mail: jwhuang@uestc.edu.cn; xfwang87@uestc.edu.cn;
jiexiong@uestc.edu.cn
H. Fang, L. Ma, J. L. Wang
School of Physics
Southeast University
Nanjing 211189, China

C. L. Zhao, J. G. Wu
Department of Materials Science
Sichuan University
Chengdu 6110064, China
C. L. Zhao
College of Materials Science and Engineering
Fuzhou University
Fuzhou 350108, China
N. Z. Shang, K. H. Liu
State Key Laboratory for Mesoscopic Physics
Frontiers Science Center for Nano-optoelectronics
School of Physics
Academy for Advanced Interdisciplinary Studies
Peking University
Beijing 100871, China

 The ORCID identification number(s) for the author(s) of this article can be found under <https://doi.org/10.1002/adma.202204697>.

DOI: 10.1002/adma.202204697

Therefore, suppressing the elemental segregation at the interface between switch unit, memory unit and the electrodes is the most critical to realize a robust and reliable memory cell.

In recent study, elementary Te is found to be the only peculiar material that can be used for switch unit without segregation.^[23] However, inevitable compositional and structural inhomogeneity resulted from elemental segregation in memory unit still challenges the reliability of the whole memory cell. A new architecture of crossbar-array memory cell with Te for both memory and switch units can be expected to realize compositional and structural homogeneities of the whole memory structure during cycling and increase the integration density of electronics. It is regrettable that although many extraordinary electronic, optical, mechanical, and thermal related properties are achieved in 2D-Te-based devices,^[24–34] the experimental work on memory function of pure 2D Te has not been reported yet. Piezoelectricity with spontaneous polarization is one option to fabricate memory device, and previous theories predicted that 2D Te is piezoelectric^[35] with polarization of $90 \mu\text{C cm}^{-2}$, and ferroelectric^[36] with electric polarization of $1.02 \times 10^{-10} \text{ C m}^{-1}$, providing probability to build high-performance memory, but no experiment was confirmed. On one hand, a non-centrosymmetric structure is typically demanded in piezoelectrics/ferroelectrics, which is induced by different long-range Coulombic interaction and inhomogeneous charge density in different atoms.^[37] On the contrary, the electronegativity of each atom in most elementary materials is expected to be equal and the structure is highly symmetric. On the other hand, large dominated leakage current is inevitable due to the gap-less nature of the most elementary materials, challenging the observation of the polarization behavior via conventional method. Therefore, it is of vital importance to give experimental evidence for the state of the piezoelectricity with reliable spontaneous polarization in 2D Te to build robust and reliable memory.

In this work, robust room-temperature in-plane and out-of-plane piezoelectricity with reliable spontaneous polarization in 2D elementary Te even monolayer tellurene (0.4 nm) are clearly observed experimentally and analyzed synthetically. The reason can be concluded as the highly oriented polarization of the molecular structure and the non-centrosymmetric lattice structure of Te, which lead to many anisotropic and spontaneous polarization behavior. The piezoelectric coefficient d_{33} is measured to be 20 pm V^{-1} and the high thermal stability with a Curie temperature of about 600 K is confirmed. The piezo response in monolayer tellurene is stable and has strong endurance to ambient air condition, as the switchable piezoelectric states can be retain for 16.5 h and are still reprogrammable even after being kept in ambient air for 10 months, which overcomes the common instability of almost 2D monolayer piezoelectrics. The 2D-Te-based field effect transistor (FET) with charming memory window (7000) and low working voltage (2 V, with $V_{\text{DS}} = 100 \text{ mV}$) are further fabricated for potential application in low-power neuromorphic computing. In the Te-based diode, a high on switching current up to $36.6 \mu\text{A} \mu\text{m}^{-1}$ without top-gate is realized. The memory behavior in the Te-based FET and diode provide a chance to eliminate the elemental segregation in memory cell by integrating memory unit and switch unit into one single device using pure Te, inspiring the novel architecture for robust and reliable memory.

2. Results and Discussion

2.1. Characterization of Tellurene and Few-Layer Te

Te is composed of unique helical chiral chains along *c*-axis, which stack in hexagonal array via van der Waals force (Figure 1a; Figure S1, Supporting Information).^[24] Due to the unique asymmetric structure, Te shows strong optical and electronic anisotropy. The X-ray diffraction (XRD) pattern in Figure S2 (Supporting Information) demonstrates the high purity and crystallinity of the as-synthesized 2D Te. The X-ray photoelectron spectroscopy (XPS) spectrum confirms the state of Te (Figure S3, Supporting Information). Two peaks located at 572.7 and 572.9 eV in the Te $3d_{5/2}$ spectrum are defined as Te^0 and suboxide state, respectively, and no signal of Te^{4+} species or other states are observed. The suboxide state is resulted from the interaction of Te atoms and adsorbed O atoms, which is also known as transient species.^[38] The results confirm the elemental purity of Te. Moreover, high-resolution transmission electron microscopy (HRTEM) image and selected-area electron diffraction (SAED) pattern in Figure S4 in the Supporting Information confirm the single crystal property of as-obtained Te. The thickness-dependent Raman spectra (Figure S5, Supporting Information) show obvious sharp peaks for bulk 2D Te and monolayer tellurene, also evidence the good crystal quality of Te. Four peaks located at 89.5 cm^{-1} (E_1 -TO mode), 101.5 cm^{-1} (E_1 -LO mode), 120.9 cm^{-1} (A_1 mode), and 138.8 cm^{-1} (E_2 mode) can be observed for 10 nm-thick 2D Te (the vibration is shown in Figure S6 in the Supporting Information). As the thickness decreases, the E_1 -LO mode shows a redshift, while A_1 and E_2 modes demonstrate a significant blueshift, which correspond well with the previous reports.^[24,26] Due to the unique chain structure, the interchain van der Waals interaction and intrachain covalent interaction are enhanced with the decrease of thickness, leading to stronger restoring force of Te atoms. Hence, the out-of-plane A_1 mode shows anomalous identical Raman shift sensitivity to the thickness of Te.^[39] The thickness of Te is measured by the atomic force microscopy (AFM), and the minimum value of which is 0.47 nm according to AFM height profile (Figure S7, Supporting Information), indicating the successful synthesis of monolayer Te, namely tellurene.

The symmetry and polarization of Te were explored by using angle-resolved polarized Raman spectroscopy (ARP Raman). Figure 1b presents the Raman spectra of 2D Te (thickness $\approx 20 \text{ nm}$) nanoflake at configuration of 0 degree under un-, parallel-, and perpendicular-polarized Raman scattering. The intensity of E_1 -TO, A_1 and E_2 modes show different polarization behavior that the tendency becomes weaker or stronger under different configuration. To investigate the asymmetric behavior of 2D Te flakes, angle resolved Raman spectra were analyzed (Figure 1c,d; Figures S8 and S9, Supporting Information). An obvious anisotropic Raman behavior is observed, where the intensity of E_1 -TO mode and A_1 mode show two-lobe shape, and the intensity of E_2 mode shows four-lobe shape at parallel configuration (Figure 1c). When the polarization configuration turns to be perpendicular, all of the modes show four-lobe shape (Figure 1d). We define anisotropic Raman ratio as maximum Raman tensor intensity divided by the minimum, the ratio is calculated to be 35.3, 3.4, and 17.1 at parallel polarization,

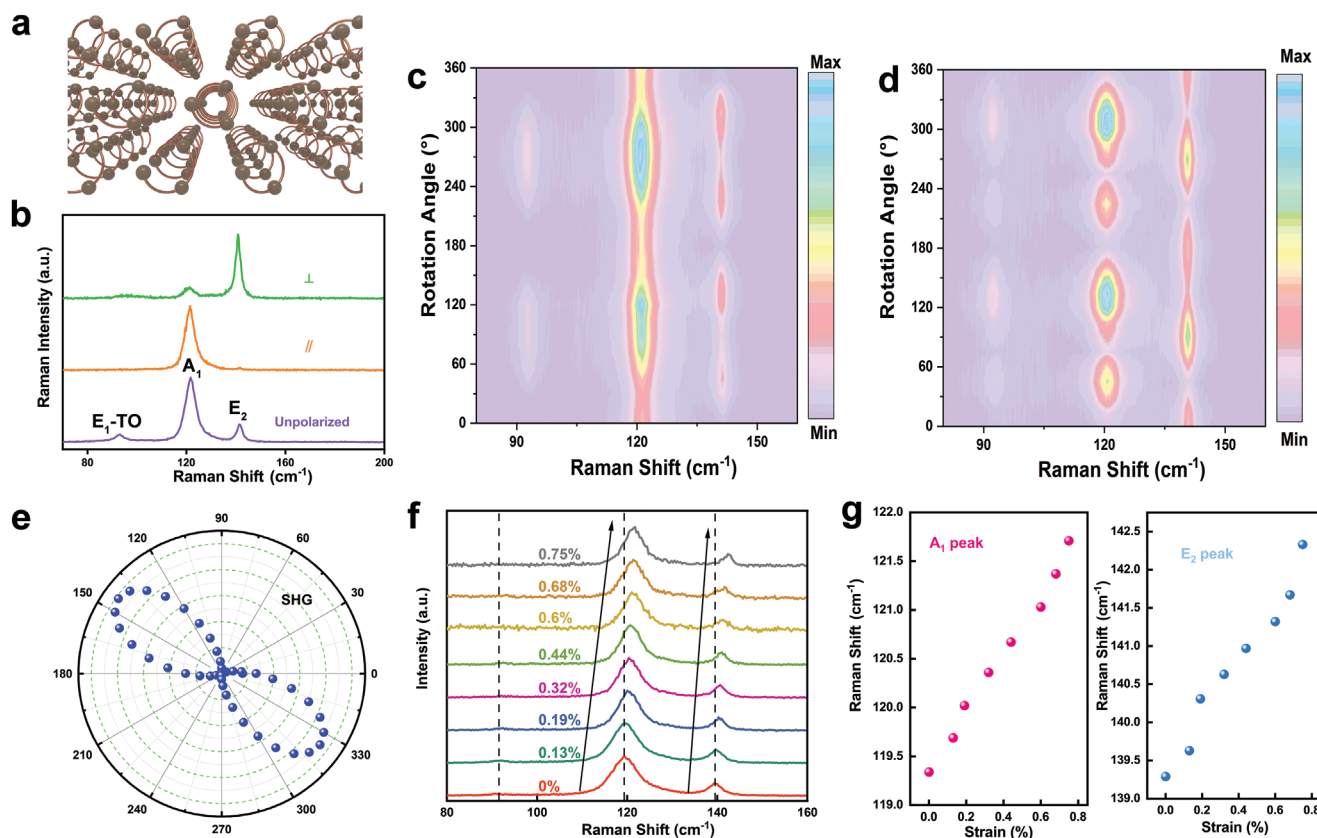


Figure 1. Anisotropic characterization of Te. a) Unique helical chiral-chain structure of Te. b) Normalized Raman spectrum at configurations of unpolarized, parallel-polarized, and perpendicular-polarized Raman along [0001]. c,d) Parallel- and perpendicular-polarized angle-resolved Raman intensity in a colored plot. e) Polar plot for total SHG intensity of Te. f) Raman spectra under tensile strain. g) Raman shift of A_1 peak and E_2 peak under strain.

13.5, 16.7, and 6.9 at perpendicular polarization for E_1 -TO mode, A_1 mode and E_2 mode, respectively. These high values of the Raman ratio indicate the strong anisotropic property of 2D Te. Angle-resolved Raman spectra of Te with thickness of 10 and 4 nm also demonstrate the same anisotropic Raman behavior (Figures S10–S13, Supporting Information), revealing the thickness-independent symmetry and polarization of Te. The anisotropic property was further confirmed by the angle-resolved second-harmonic-generation spectroscopy (SHG), which is sensitive to the polarization and structure asymmetry in materials.^[40] The polar plot of the in-plane total SHG intensity (Figure 1e) shows two-lobe symmetry, indicating the poor structure symmetry in 2D Te.^[41–43]

To further understand the anisotropic property, in situ strain-modulated Raman test on Te was carried out (Figure 1f,g; Figure S14, Supporting Information). When the force is applied perpendicular to the chain, an obvious blueshift is found for A_1 and E_2 modes, while the E_1 -TO mode remains unchanged. The reason can be ascribed to the decreased bond angle (θ) and increased distance (l) under tensile strain (Figure S6, Supporting Information), which can enhance the vibration of A_1 and E_2 modes but do not affect the vibration of E_1 -TO mode. The peak positions of A_1 and E_2 modes along with the applied strain are displayed in Figure 1g. The external strain field shows anisotropic affection to the lattice, which further confirms the strong anisotropic property of 2D Te. These results clearly

demonstrate high structural asymmetry of Te, leading to anisotropic property including polarization. Many extraordinary properties can be expected in asymmetric system, like charming ferromagnetism, ferroelectricity and piezoelectricity.^[44]

2.2. Theoretical Calculations and Symmetry Analysis

In order to understand the anisotropic property of Te deeply, first-principle calculations were then carried out. The charge density difference is used to describe the difference between the bond charge density and the atomic charge density, giving some insight of the electrons- or holes-distribution around the ion. Through the differential charge density, it is possible to clearly obtain the properties of the charge movement and the potential polarization direction of the bond during the bonding formation and the dipole coupling process.^[45] The charge density difference of Te at the conduction band minimum (CBM) and valence band maximum (VBM) are shown in Figure 2a,b. From VBM states, strong intrachain covalent interaction bonding can be viewed. Moreover, the charge density difference shows large asymmetry of electronic distribution, which will lead to large electric dipole and result in electrical polarization. The nonspherical electronic occupied state in Figure 2a reveals a dipole polarization state in the material, which provides objects to investigate the piezoelectricity

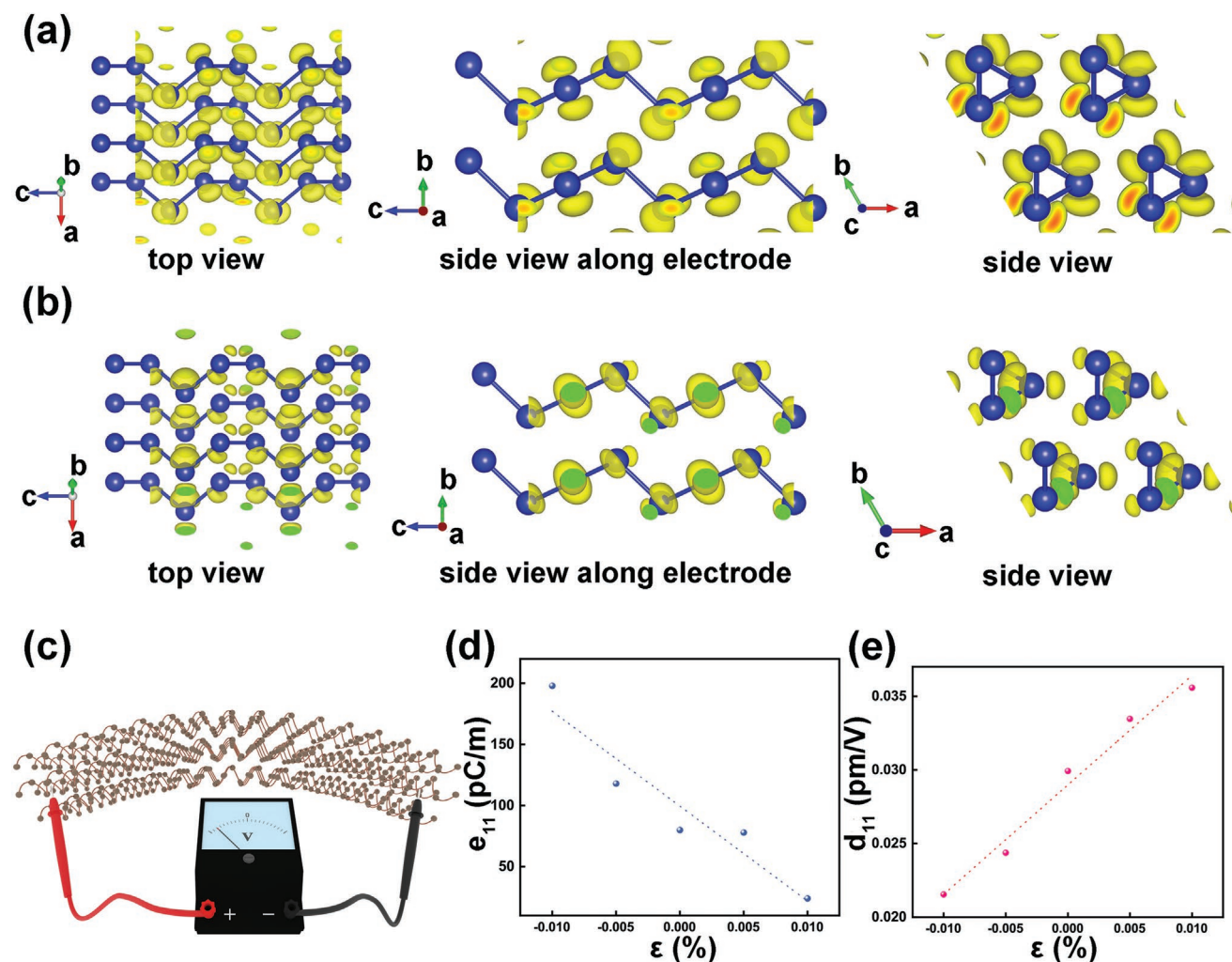


Figure 2. Atomic structure and piezoelectric calculation of Te. a,b) Charge density difference at VBM (a) and CBM (b) of α -Te. c) Schematic for piezoelectric response of Te. d) Different e_{11} coefficients with strain and e) different d_{11} coefficients with strain.

with spontaneous polarizations in Te. In this structure, more charges are transferred to side Te from two arm atoms, leading to preferential charges along b and c axis. This imbalance breaks the intrinsic symmetry of lattice structure, resulting in lower in-plane and out-of-plane symmetry in 2D Te. Herein, 2D Te films own non-zero value of e_{11}/d_{11} and e_{33}/d_{33} , which means both in-plane and out-of-plane piezoelectric polarization are allowed under uniaxial strain (as shown in Figure 2c).

The relaxed ion elastic and piezoelectric tensors are obtained as the sum of ionic and electronic contributions. Piezoelectric tensor is contributed by both ionic and electronic deviation and dipole variation, which is defined by^[46]

$$C_{ijkl} = \frac{d\sigma_{ij}}{d\varepsilon_{kl}} = C_{ijkl}^{\text{el}} + C_{ijkl}^{\text{ion}} \quad (1)$$

$$e_{ijk} = \frac{dP_i}{d\varepsilon_{jk}} = e_{ijk}^{\text{el}} + e_{ijk}^{\text{ion}} \quad (2)$$

where σ_{ij} is the stress tensor, ε_{kl} is the strain tensor, and P_i is the intrinsic polarization tensor. In 2D systems, we assume Z

direction as $\varepsilon_{ij} = \sigma_{ij} = 0$ for $i = 3$ or $j = 3$.^[46] Then the 2D elastic and piezoelectric tensors become^[47]

$$C_{ij} = \begin{pmatrix} C_{11} & C_{12} & C_{16} \\ C_{21} & C_{22} & C_{26} \\ C_{61} & C_{62} & C_{66} \end{pmatrix} \quad (3)$$

$$e_{ij} = \begin{pmatrix} e_{11} & e_{12} & e_{16} \\ e_{21} & e_{22} & e_{26} \\ e_{31} & e_{32} & e_{36} \end{pmatrix} \quad (4)$$

2D Te belongs to $P3_121$ point group with D_3 symmetry. We derive the expressions of the independent d_{ij} coefficients for this point group. Then the elastic and piezoelectric tensors become^[48,49]

$$C_{ij} = \begin{pmatrix} C_{11} & C_{12} & C_{13} & C_{14} & C_{15} & 0 \\ C_{12} & C_{11} & C_{13} & -C_{14} & C_{25} & C_{26} \\ C_{13} & C_{13} & C_{33} & 0 & C_{15} & 0 \\ C_{14} & -C_{14} & 0 & C_{44} & 0 & C_{46} \\ C_{15} & C_{25} & C_{15} & 0 & -C_{25} & C_{14} \\ 0 & C_{26} & 0 & C_{46} & C_{14} & C_{66} \end{pmatrix} \quad (5)$$

$$e_{ij} = \begin{pmatrix} e_{11} & -e_{11} & 0 & e_{14} & e_{15} & 0 \\ 0 & 0 & 0 & e_{24} & 0 & e_{26} \\ e_{31} & e_{31} & e_{33} & 0 & 0 & 0 \end{pmatrix} \quad (6)$$

$$d_{ij} = \begin{pmatrix} d_{11} & -d_{11} & 0 & d_{14} & d_{15} & 0 \\ 0 & 0 & 0 & d_{24} & 0 & d_{26} \\ d_{31} & d_{31} & d_{33} & 0 & 0 & 0 \end{pmatrix} \quad (7)$$

Combining these equations, we can solve the piezoelectric coefficients

$$e_{ii} = d_{ik} C_{ik} \quad (8)$$

$$d_{11} = \frac{e_{11}}{C_{11} - C_{12}} d_{31} = \frac{e_{31}}{C_{11} + C_{12}} \quad (9)$$

Te is demonstrated to be a non-centrosymmetric lattice structure with highly oriented polarization of molecular structure. Theoretically, the absence of both the inversion symmetry and out-of-plane mirror symmetry, together with stretchable mechanical properties, lead to large in-plane and out-of-plane piezoelectric performance. The piezoelectric coefficient of tellurene was calculated by considering the lattice structure symmetry of single-layer tellurene and Equations (1,2,8,9).

We obtain e_{ij} for tellurene via fitting piezoelectric polarization with uniaxial strain. The d_{11} of 0.03 pm V⁻¹ for monolayer tellurene, and high d_{33} of 15 pm V⁻¹ for bilayer tellurene (shown in Figure 2d,e; Table S1, Supporting Information) are obtained. Moreover, it is interesting that the piezoelectric behavior can be modulated by strain. The nearly linear relationship between e_{11} and d_{11} and strain are observed, which means that Te has potential application in high-density flexible force sensors to identify tensile and compressive forces.

Besides, the density functional theory (DFT) simulations also suggest the existence of spontaneous dipole polarization in α -Te, which imply the ferroelectric nature of piezoelectric Te. As shown in Figure S15 (Supporting Information), there are two polar-axis direction in α -Te. One is along the c axis ([0001] direction), which is also parallel to electrical fields of source and drain electrode, and contributes mainly to in-plane polarization. The other is along the b direction (90° to the c axis and 120° to the a axis); the polar vector has two field vectors, which contribute to the out-of-plane and in-plane spontaneous polarization, respectively. These results confirm the piezoelectricity and weak ferroelectric nature theoretically. However, for gap-less semiconductors and semimetals, it is hard to directly detect the original ferroelectric domain wall via conventional methods.^[50]

2.3. Piezoelectricity and Spontaneous Polarization Behavior in Te and Tellurene

The existence of piezoelectricity requires electrical dipole switching under force. To characterize the state of electrical dipole of tellurene at nanoscale, piezoresponse force microscopy (PFM) measurement was performed. In the process of PFM test, the conductive tip oscillates in contact with the surface, then the first harmonic component signal is detected to reflect surface electromechanical deformation. The deflection

amplitude is proportional to the piezoelectric coefficient, and the phase gives information about polarization direction. Figure 3a,b shows out-of-plane PFM phase and amplitude image of monolayer tellurene after 4 V lithography (AFM height profile is shown in Figure S16 in the Supporting Information). An 180° phase contrast is observed, confirming the piezoelectric nature. To test the stability to maintain the dipole state, long-time dependent PFM phase images were collected as shown in Figure S17 in the Supporting Information. After being exposed in ambient condition for 16.5 h, the contrast of the area with different phase is still clearly observed, showing good retention capability. Such a long-term retention suggests that the PFM contrast is ascribed to the piezoelectric behavior rather than the shorter-scale spurious effects.^[51] Moreover, the sample was rewritten after being kept in ambient air for 10 months, the contrast of PFM phase (Figure S18, Supporting Information) is still identical clearly, demonstrating ultrastrong structure stability in air, which is a good merit compared with other piezoelectric atomic 2D materials. Besides, local PFM switching spectroscopy loop further confirms the robust piezoelectricity of Te, as demonstrated by readily apparent 180° phase hysteresis and its butterfly-shape amplitude (d_{33}) loop in Figure 3c. During the local PFM switching test, PFM spectroscopy is performed with gold electrode upon tellurene to avoid electrostatic artefacts from the tip and potential electromechanical contributions.^[52,53] In this experiment, d_{33} is calculated to be 20 pm V⁻¹, demonstrating obvious piezoelectric property (details is shown in Note S3, Piezoelectric Force Microscopy Measurements, in the Supporting Information). The PFM phase image of 20 nm-thick Te shown in Figure S19 in the Supporting Information also demonstrates the robust piezoelectricity in thick 2D Te.

It is worth noting that PFM tip can only impose out-of-plane electric field, which is difficult to detect in-plane piezoelectric switching behavior. To demonstrate the in-plane piezoelectric behavior and spontaneous polarization of tellurene, two-terminal in-plane electrode device is fabricated using Ag/Au (20 nm/30 nm) as electrode. The I_d - V_d curves are shown in Figure 3d. A large hysteresis loop is observed with the maximum conductance at V_d of 1.5–2.0 V for 1.6 nm-thick tellurene flake. This loop confirms the polarization switching of dipole, demonstrating room-temperature in-plane piezoelectricity and spontaneous polarization induced hysteresis behavior of tellurene.^[54] Besides, the on current during the switch achieves as high as 36.6 $\mu\text{A } \mu\text{m}^{-1}$ without top-gating, suggesting the potential application for low-power and high-speed non-volatile memory applications. The unstable current observed in Figure S20 in the Supporting Information for monolayer tellurene is probably caused by adsorbates on monolayer surface and poor adhesion of Ag electrode,^[55] which affect the contact property of tellurene with Ag electrode.

To evaluate the potential electronic application of semiconducting piezoelectric tellurene, the two-terminal transistor using pure piezoelectric Te as channel with 300 nm SiO₂ back gate was fabricated (the schematic structure map is shown in Figure S21 in the Supporting Information). A counterclockwise hysteresis loop with large memory window of 7000 is realized (Figure 3e), showing ability to build high-performance memory device. It is known that the hysteresis loop is not counterclockwise if there are large charge trapping processes

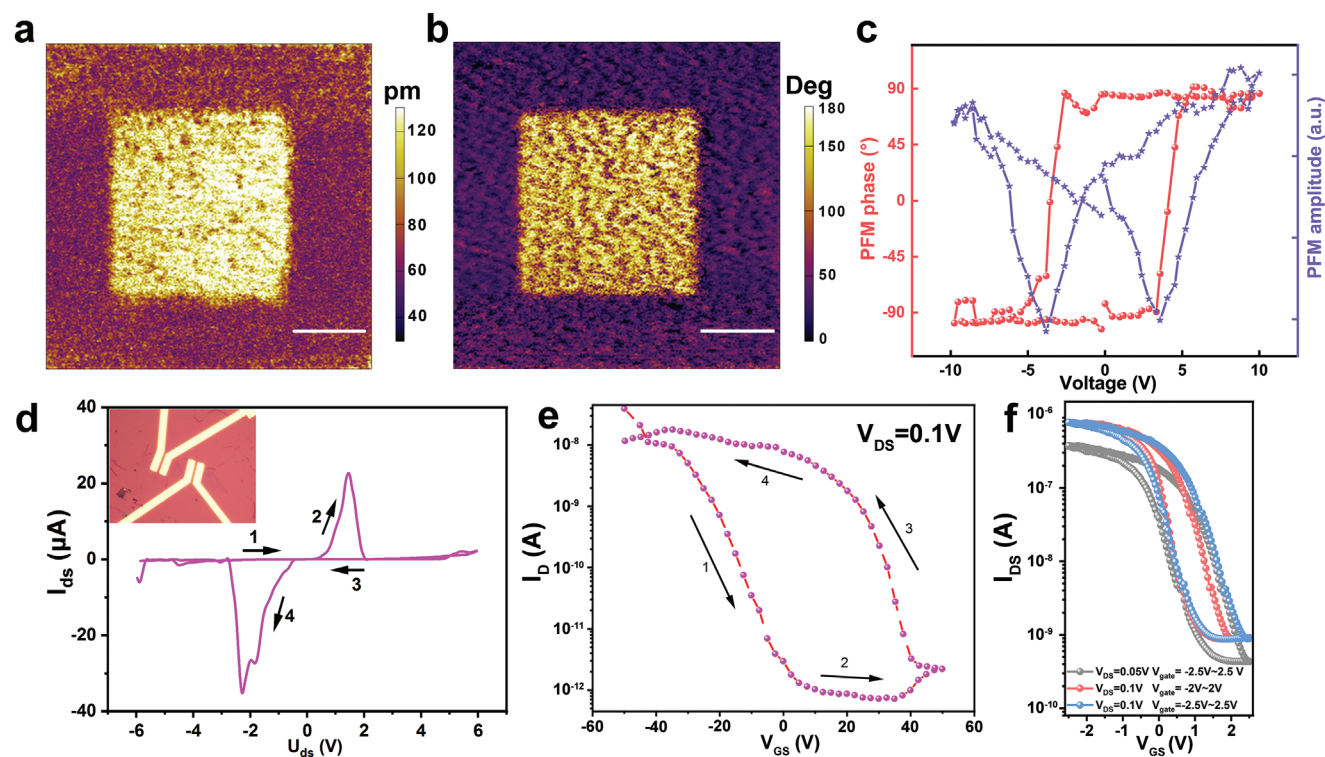


Figure 3. Evidence for piezoelectricity and piezoelectric transistor behavior in Te. a,b) PFM amplitude and phase image of monolayer tellurene with ± 4 V writing voltage at room temperature. c) PFM phase hysteresis and butterfly loops of 4 layers of tellurene. d) In-plane piezoelectric resistive switching for 1.6 nm-thick tellurene flakes. e) Piezoelectric transistor for 2 nm tellurene flakes on the SiO_2 back gate. f) Piezoelectric transistor on the HfO_2 back gate. Scale bar: 1 μm .

in the loop. So that the hysteresis loop is mainly induced by piezoelectricity with spontaneous polarization which further confirm the piezoelectric nature of 2D Te, showing interesting ferroelectric like hysteresis behavior in the device.^[56] To gain a lower work voltage for low-power-consumption electronics, we also characterized the Te-based transistor on 10 nm-thick high-dielectric HfO_2 back-gated substrate, as shown in Figure 3f. The working gate voltage can be as low as 2 V with $V_{\text{DS}} = 100$ mV, which potentially provides a path for high-performance transistors with memory function. A series switching characteristics of tellurene field-effect transistors on a high- k HfO_2 dielectric layer is carried out via different V_{gs} and V_{ds} at 12 tellurene flakes (the data are shown in Figure S22 in the Supporting Information). The lowest working gate voltage is observed at ≈ 1 V with $V_{\text{DS}} = 1$ V, with on/off ratio ≈ 7 orders and memory window ≈ 300 (Figure S22i, Supporting Information). Besides, the $I_{\text{DS}}-V_{\text{DS}}$ curves show good Schottky contact property. Herein, the results inspire a new architecture to build cross-bar memory array using pure Te, merging both memory and switch function in a single Te-based device, which can greatly improve the integration density and bring high compositional and structural homogeneity.

To uncover the polarization behavior of dipoles in piezoelectric 2D Te, systematic deep SHG test was further performed (Figure 4a), which has been applied as a powerful tool to examine crystal orientation, strain-induced deformation and magnetic or electric polarization, etc., due to its prominent sensitivity to symmetry and crystal structure. Here we collected

SHG signal of tellurene with thickness from monolayer to tetralayer (Figure 4b). All the spectra show SHG peak at 532 nm, revealing the non-centrosymmetric and strong anisotropic property of Te even the monolayer tellurene. The second-order nonlinear optical polarization is given as^[57]

$$P_i(2\omega) = \epsilon_0 \hat{\chi}_{ijk}^{(2)} E_j(\omega) E_k(\omega) \quad (10)$$

$$\hat{\chi}^{(2)}(\pm P) = \pm P \hat{\chi}_0^{(2)} \quad (11)$$

where ϵ_0 is the vacuum permittivity, $\hat{\chi}_{ijk}^{(2)}$ is the second-order nonlinear coefficient tensor, and $E(\omega)$ is the electric field of incident light. For an electric dipole model, the reduced symmetry leads to the substantial dependence of $P_i(2\omega)$ to the electric dipole moment, which makes the SHG signal sensitive to the piezoelectric polarization. Besides, SHG is a noninvasive probing for electric orders as no external electric field is introduced compared with traditional PFM method, so that the intrinsic polarization state can be obtained without affection of extra voltage. Thus, we then carried out SHG mapping measurement of a few-layer Te sample to further examine the electric dipole polarization as a complement to PFM examination. The SHG intensity mapping shows anomalous inhomogeneous response in one flake (Figure 4c), the two typical regions marked as point one and two are further investigated via angle-resolved SHG shown in Figure 4d–g. As witnessed in Figure 4e,g, the crystal orientation at point one and two show small angle difference but large intensity difference.

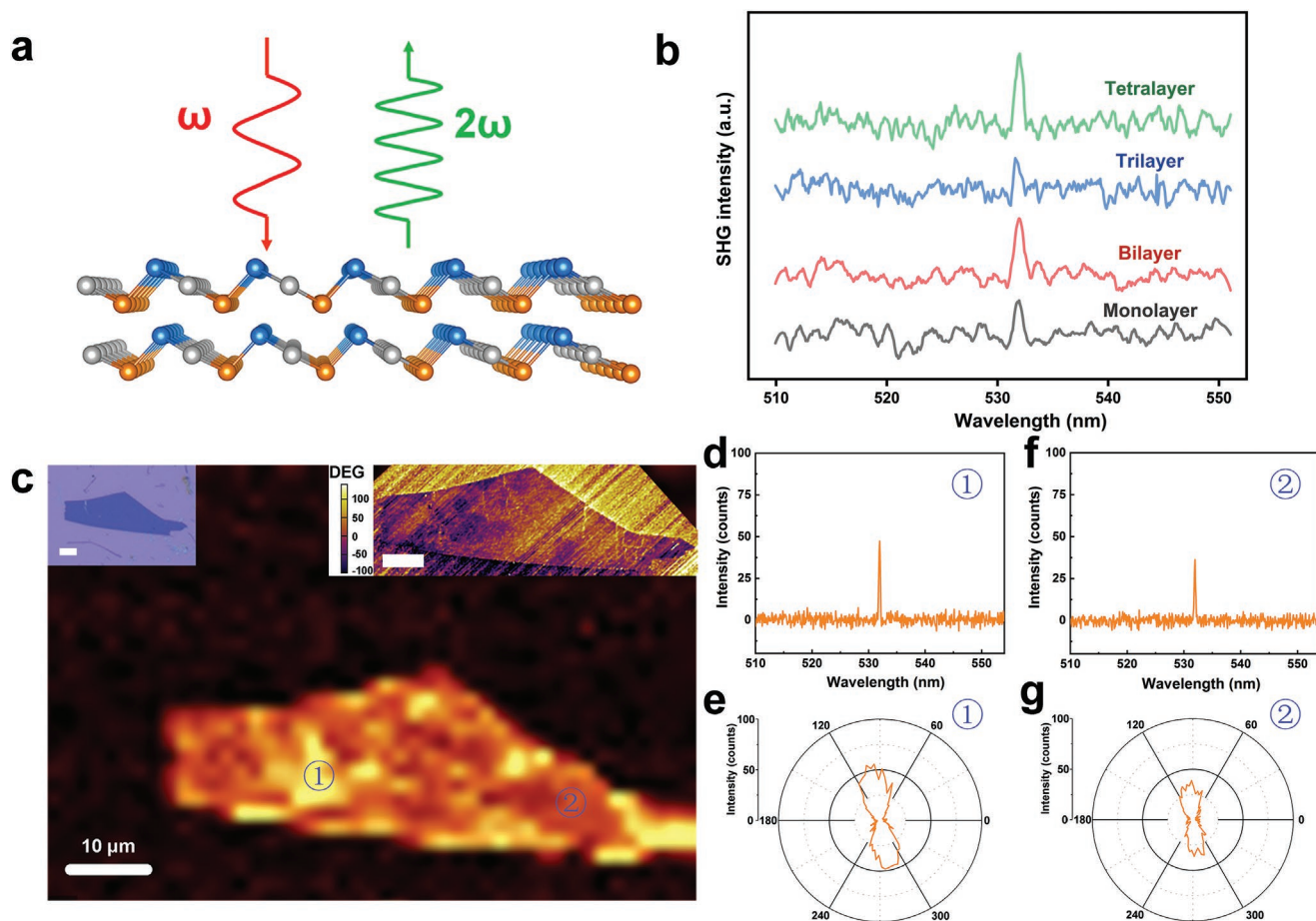


Figure 4. SHG characterization for spontaneous polarization in Te. a) Schematic diagram for SHG test for Te. b) SHG spectra of 1–4-layer tellurene. c) SHG mapping of Te flakes, the inset image in left and right side are the optical and PFM phase images, respectively. d, e) SHG spectrum and angle-resolved plot at point 1. f, g) SHG spectrum and angle-resolved plot at point 2, the slight angle-difference of the plots indicates different dipole polarization. The scale bar is 10 μm .

Typically, this phenomenon can be induced by inhomogeneous thickness, inhomogeneous crystallinity, or electric dipole polarizing domain. The thickness and crystallinity distribution of 2D Te were then examined using nondestructive Raman. By imaging the Raman position and full width at half maxima (FWHM) of A_1 mode which are very sensitive to thickness and crystallinity,^[58] the uniform thickness and crystallinity of the sample are clearly evidenced as no obvious contrast can be observed from the mappings (Figure S21, Supporting Information). Consequently, the inhomogeneous SHG response should be resulted from electric dipole polarizing domain. Furthermore, we carried out PFM test at the same sample, the in-plane PFM phase image (upper right in Figure 4c) shows two distinguishable domains corresponding to the two distinct SHG mapping region, further implying inhomogeneous spontaneous in-plane polarization in Te. This anomalous phenomenon could be induced by weak ferroelectric behavior. However, due to the small bandgap of Te, it is hard to detect perfect original ferroelectric domain via PFM, because of the large leakage current among the lattice.

Considering the ferroelectric nature predicted by previous theoretical result and ferroelectric behavior found in this work, we carried out PFM phase and amplitude test upon Te at the

micrometer scale, attempting to measure the polarization domain walls. As shown in Figure S22 (Supporting Information), two areas with 180° phase contrast are observed (red line), which are not correlated with topography, revealing the piezoelectric Te shows some ferroelectric nature. However, the boundary is undistinguishable due to the large current leakage from the lattice.^[50] The polarization-field ferroelectric loop shown in Figure S25 (Supporting Information) is also not definitive, due to leakage current. Besides, we also carried out in situ Raman processing with sweeping of gate voltage (results and details are shown in Figure S23 in the Supporting Information). The result reveals that the lattice structure is strongly correlated with gate voltage further confirm the piezoelectric behavior and spontaneous polarization of 2D Te. Above all, we systematically investigated and demonstrated the robust piezoelectricity in 2D Te even the thickness is down to 0.4 nm from multiapproaches.

2.4. Thermal Stability

Thermal stability at high temperature is a key merit for high-performance memory during cycling. To judge the stability of piezoelectric Te at high temperature, the dipole polarization and

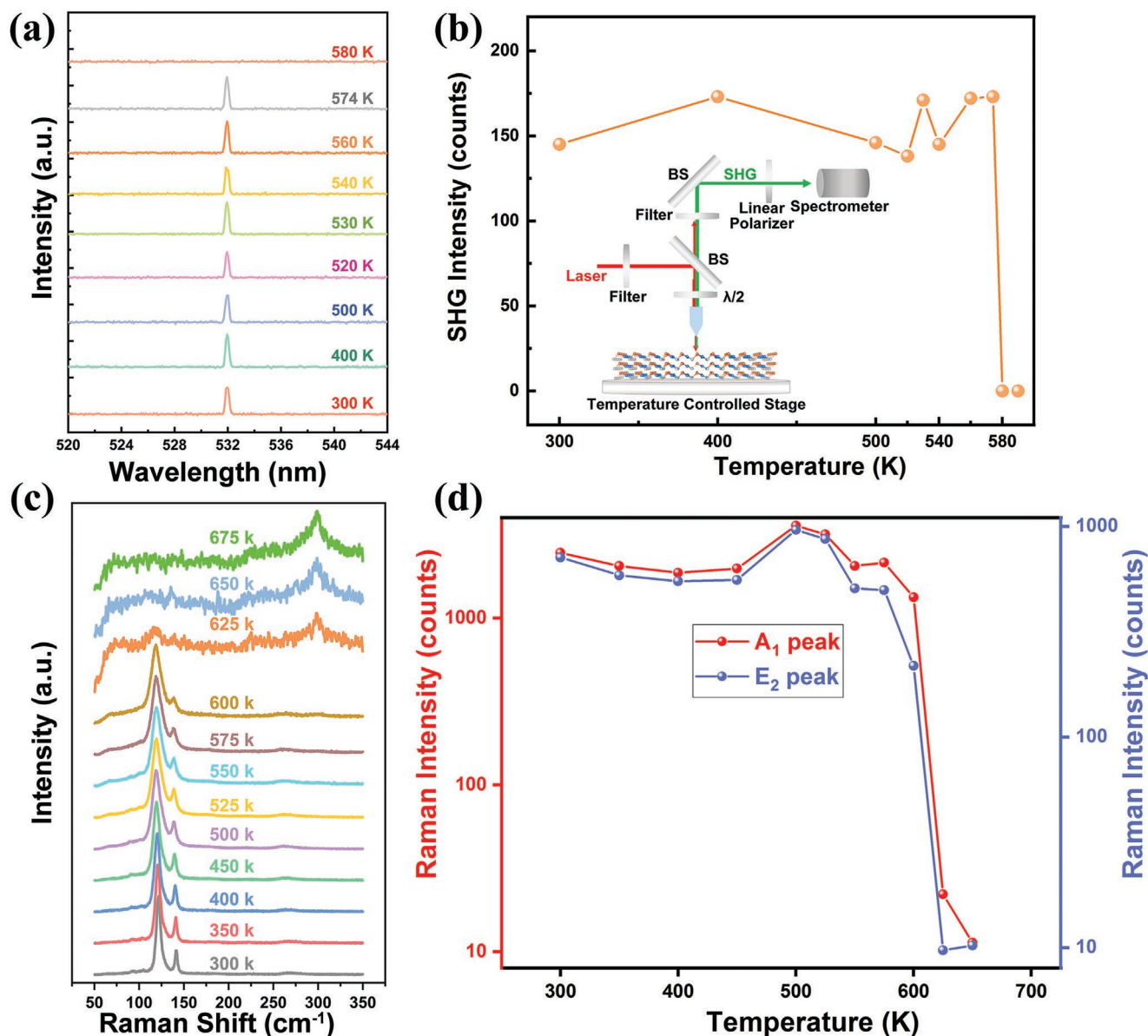


Figure 5. Observation of temperature-dependent polarization and structure stability. a,b) Temperature-dependent SHG spectra and plot of SHG intensity at different temperature. c,d) Temperature-dependent Raman spectra (normalized by highest peak) and plot of Raman intensity of A_1 and E_2 mode at different temperature.

structure stability were further examined via in situ temperature-dependent SHG and Raman spectroscopy. Conventionally, high thermal fluctuations will occur under high temperature, which would destabilize the dipole polarization and drive the structure into high-symmetry paraelectric phase with inversion symmetry.^[59] In the result of temperature-dependent SHG, a gradual intensity change can be observed before 560 K, confirming the robust dipole polar order and asymmetric structure (Figure 5a,b). When the temperature is increased above 574 K, a sharp drop of SHG intensity is observed, indicating a rapid dipole depolarization as the piezoelectric phase transforms into high symmetric paraelectric phase. The high transition temperature is attributed to the stable structure of Te, as well as the large kinetic transition barrier from piezoelectric

structure to high symmetric paraelectric structure. Moreover, temperature-dependent Raman was also carried out to further investigate the thermal structure stability (Figure 5c,d). Both Raman intensity of A_1 and E_2 modes are stable before 575 K while a rapid decrease occurs when the temperature is up to 600 K, showing very stable structure at high temperature. Besides, considering the harmful effect of blackbody radiation induced by high temperature to the Raman signal, a violet laser at 325 nm wavelength was equipped in the Raman instrument to retest the thermal stability (shown in Figures S26 and S27 in the Supporting Information). All the tellurene films show ultrahigh thermal stability above 600 K, even above 725 K. Both the results demonstrate the Curie temperature of piezoelectric 2D Te is about 580–600 K, which is much higher than that of

the most of predicted 2D piezoelectric materials and reported piezoelectric materials.

3. Conclusion

We have experimentally demonstrated robust in-plane and out-of-plane piezoelectricity with spontaneous polarization in elementary monolayer tellurene at room temperature. The unique helical chain structure and highly oriented polarization of molecular structure lead to large electronic dipole and spontaneous in-plane and out-of-plane polarization. Compared to most of the reported piezoelectric 2D materials, tellurene owns ultrahigh air stability that piezoelectric structure can be maintained at least 10 months in air. The 2D-Te-based FET realizes large memory window (7000) and low work voltage (2 V) and the on switching current achieves up to $36.6 \mu\text{A}\mu\text{m}^{-1}$ without top-gate. By systemic temperature-dependent SHG and Raman measurement, the stable thermal stability with high Curie temperature of ≈ 600 K is revealed. This discovery provides a chance to redesign architecture of crossbar-array memory using pure Te, merging memory and switching function in single device without composition segregation and providing a new platform to construct vdW Waals piezoelectric heterostructures for high-density electronics.

4. Experimental Section

Crystal Characterization: The angle-resolved Raman spectra were measured via a Raman spectrometer (HR Evolution, Horiba) with 633 nm laser incident; the linear polarizers were set in front of the sample and spectrometer. The half-wave plate was set in the path to rotate the incident direction in steps of 15° to measure the angle-resolved Raman spectra. The in situ FET Raman was carried out on a SmartRaman confocal-micro-Raman module under backscattering geometry. The SmartRaman module was developed by the Institute of Semiconductors, Chinese Academy of Sciences, and was coupled with a Horiba iHR550 spectrometer and a charge-coupled device (CCD) detector. An all-fiber ultrafast laser source served as the incident light in the spectrometer (Alpha 300R, WITec) to examine the second-harmonic generation (SHG) signals of the samples; the incident wavelength was 1064 nm and the pulse width was ≈ 1 ps. The chemical composition and chemical state were tested by X-ray diffraction (XRD, Ultima IV, Rigaku), X-ray photoelectron spectroscopy (XPS, AXIS SUPRA+, SHIMADZU). Microstructure and selected-area electron diffraction were carried out via transmission electron microscopy (TEM, Tecnai, FEI). PFM measurements were performed using a commercial atomic force microscope (MFP-3D, Asylum Research,) on gold substrate; a conductive Pt-Ir coated cantilever (EFM-10, Nano World, Asylum Research) was applied. The local piezoresponse hysteresis loops were recorded by spectroscopy piezoresponse force microscopy (SS-PFM), using a triangular-wave voltage.

Device Fabrication and Characterization: All the devices were fabricated by electron beam lithography; the conductive electrodes were deposited using thermal evaporation (Suzhou Fangsheng FS-450) with Cr/Au (5 nm/50 nm) unless specifically mentioned. All the electrical measurements were carried out via a semiconductor characterization system (Keithley 4200) in a Probe Station (DOT, PRCBE). The electrical measurements under in situ FET Raman were also carried out in a Mini-Probe Station (Air, PRCBE). All the measurements were made at room temperature.

Synthesis Method: Na_2TeO_3 (analytical grade) and poly(vinylpyrrolidone) (PVP, analytical grade, average molecular weight 24k) were dispersed

in deionized water (33 mL) with a mass ratio of 1:5. The homogenous solution was poured into a Teflon-lined stainless-steel autoclave with 2.2 mL aqueous ammonia solution (25–28 wt%) and 1.12 mL hydrazine hydrate solution (85 wt%) as a pH regulator and reducing agent. The autoclave was then placed into oven at 180°C for 4 h and cooled down naturally. The product was washed using water for at least 3 times and transferred upon the substrate.

Supporting Information

Supporting Information is available from the Wiley Online Library or from the author.

Acknowledgements

G.F.R., and H.F. contributed equally to this work. The authors gratefully acknowledge the support from the National Key Research and Development Program of China (2021YFA0718800), the National Natural Science Foundation of China (U20A20244, 52002053, 52002050, 51972041, 12074056, 21903014, 52021001), the Sichuan Science and Technology Program (2021JDTD0010, 2019JDR00070), the Fundamental Research Fund for the Central Universities (ZYGX2020J004), and the China Postdoctoral Science Foundation funded project (2020M683280).

Conflict of Interest

The authors declare no conflict of interest.

Data Availability Statement

The data that support the findings of this study are available from the corresponding author upon reasonable request.

Keywords

2D materials, anisotropy, piezoelectricity, spontaneous polarization, tellurene

Received: May 24, 2022
Revised: June 22, 2022
Published online: August 3, 2022

- [1] R. Calarco, F. Arciprete, *Science* **2021**, 374, 1321.
- [2] E. J. Fuller, S. T. Keene, A. Melianas, Z. Wang, S. Agarwal, Y. Li, Y. Tuchman, C. D. James, M. J. Marinella, J. J. Yang, A. Salleo, A. A. Talin, *Science* **2019**, 364, 570.
- [3] Y. van de Burgt, A. Melianas, S. T. Keene, G. Malliaras, A. Salleo, *Nat. Electron.* **2018**, 1, 386.
- [4] J.-Q. Yang, R. Wang, Y. Ren, J.-Y. Mao, Z.-P. Wang, Y. Zhou, S.-T. Han, *Adv. Mater.* **2020**, 32, 2003610.
- [5] J. Torrejon, M. Riou, F. A. Araujo, S. Tsunegi, G. Khalsa, D. Querlioz, P. Bortolotti, V. Cros, K. Yakushiji, A. Fukushima, H. Kubota, S. Yuasa, M. D. Stiles, J. Grollier, *Nature* **2017**, 547, 428.
- [6] X. Yan, J. H. Qian, V. K. Sangwan, M. C. Hersam, *Adv. Mater.* **2022**, <https://doi.org/10.1002/adma.202108025>.

- [7] Y. Sun, M. Li, Y. Ding, H. Wang, H. Wang, Z. Chen, D. Xie, *InfoMat* **2022**, <https://doi.org/10.1002/inf2.12317>.
- [8] C. D. Schuman, S. R. Kulkarni, M. Parsa, J. P. Mitchell, P. Date, B. Kay, *Nat. Comput. Sci.* **2022**, *2*, 10.
- [9] D. Marković, A. Mizrahi, D. Querlioz, J. Grollier, *Nat. Rev. Phys.* **2020**, *2*, 499.
- [10] M. Davies, *Nat. Mach. Intell.* **2019**, *1*, 386.
- [11] J. Li, C. Ge, J. Du, C. Wang, G. Yang, K. Jin, *Adv. Mater.* **2020**, *32*, 1905764.
- [12] G. Cao, P. Meng, J. Chen, H. Liu, R. Bian, C. Zhu, F. Liu, Z. Liu, *Adv. Funct. Mater.* **2021**, *31*, 2005443.
- [13] T.-Y. Wang, J.-L. Meng, L. Chen, H. Zhu, Q.-Q. Sun, S.-J. Ding, W.-Z. Bao, D. W. Zhang, *InfoMat* **2021**, *3*, 212.
- [14] S. Choi, J. Yang, G. Wang, *Adv. Mater.* **2020**, *32*, 2004659.
- [15] H. Yeon, P. Lin, C. Choi, S. H. Tan, Y. Park, D. Lee, J. Lee, F. Xu, B. Gao, H. Wu, H. Qian, Y. Nie, S. Kim, J. Kim, *Nat. Nanotechnol.* **2020**, *15*, 574.
- [16] K. Roy, A. Jaiswal, P. Panda, *Nature* **2019**, *575*, 607.
- [17] C. Wang, S.-J. Liang, C.-Y. Wang, Z.-Z. Yang, Y. Ge, C. Pan, X. Shen, W. Wei, Y. Zhao, Z. Zhang, B. Cheng, C. Zhang, F. Miao, *Nat. Nanotechnol.* **2021**, *16*, 1079.
- [18] S. Jung, H. Lee, S. Myung, H. Kim, S. K. Yoon, S.-W. Kwon, Y. Ju, M. Kim, W. Yi, S. Han, B. Kwon, B. Seo, K. Lee, G.-H. Koh, K. Lee, Y. Song, C. Choi, D. Ham, S. J. Kim, *Nature* **2022**, *601*, 211.
- [19] C. Liu, H. Chen, S. Wang, Q. Liu, Y.-G. Jiang, D. W. Zhang, M. Liu, P. Zhou, *Nat. Nanotechnol.* **2020**, *15*, 545.
- [20] H. S. P. Wong, S. Raoux, S. Kim, J. Liang, J. P. Reifenberg, B. Rajendran, M. Asheghi, K. E. Goodson, *Proc. IEEE* **2010**, *98*, 2201.
- [21] D. Garbin, W. Devulder, R. Degraeve, G. L. Donadio, S. Clima, K. Opsomer, A. Fantini, D. Cellier, W. G. Kim, M. Pakala, A. Cockburn, C. Detavernier, R. Delhougne, L. Goux, G. S. Kar, in *2019 Int. Electron Devices Meeting (IEDM)*, IEEE, Piscataway, NJ, USA **2019**, <https://doi.org/10.1109/IEDM19573.2019.8993547>.
- [22] C. Laguna, M. Bernard, N. Bernier, D. Rouchon, N. Rochat, J. Garrione, A. Jannaud, E. Nolot, V. Meli, N. Castellani, C. Sabbione, G. Bourgeois, M. C. Cyrille, L. Militaru, A. Souifi, G. Navarro, E. Nowak, in *2021 International Memory Workshop (IMW)*, IEEE, Piscataway, NJ, USA **2021**, <https://doi.org/10.1109/IMW51353.2021.9439590>.
- [23] J. Shen, S. Jia, N. Shi, Q. Ge, T. Gotoh, S. Lv, Q. Liu, R. Dronskowski, S. R. Elliott, Z. J. S. Song, *Science* **2021**, *374*, 1390.
- [24] Y. Wang, G. Qiu, R. Wang, S. Huang, Q. Wang, Y. Liu, Y. Du, W. A. Goddard, M. J. Kim, X. Xu, P. D. Ye, W. Wu, *Nat. Electron.* **2018**, *1*, 228.
- [25] G. Jnawali, Y. Xiang, S. M. Linser, I. A. Shojaei, R. Wang, G. Qiu, C. Lian, B. M. Wong, W. Wu, P. D. Ye, Y. Leng, H. E. Jackson, L. M. Smith, *Nat. Commun.* **2020**, *11*, 3991.
- [26] J.-K. Qin, P.-Y. Liao, M. Si, S. Gao, G. Qiu, J. Jian, Q. Wang, S.-Q. Zhang, S. Huang, A. Charnas, Y. Wang, M. J. Kim, W. Wu, X. Xu, H.-Y. Wang, L. Yang, Y. Khin Yap, P. D. Ye, *Nat. Electron.* **2020**, *3*, 141.
- [27] C. Zhao, C. Tan, D.-H. Lien, X. Song, M. Amani, M. Hettick, H. Y. Y. Nyein, Z. Yuan, L. Li, M. C. Scott, A. Javey, *Nat. Nanotechnol.* **2020**, *15*, 53.
- [28] Y. Wang, S. Yao, P. Liao, S. Jin, Q. Wang, M. J. Kim, G. J. Cheng, W. Wu, *Adv. Mater.* **2020**, *32*, 2002342.
- [29] G. Qiu, S. Huang, M. Segovia, P. K. Venuthurumilli, Y. Wang, W. Wu, X. Xu, P. D. Ye, *Nano Lett.* **2019**, *19*, 1955.
- [30] B. Zhu, Q. Chen, S. Jiang, M. Holt, W. Zhu, D. Akinwande, L. Tao, *InfoMat* **2021**, *3*, 271.
- [31] L. Tong, X. Huang, P. Wang, L. Ye, M. Peng, L. An, Q. Sun, Y. Zhang, G. Yang, Z. Li, F. Zhong, F. Wang, Y. Wang, M. Motlag, W. Wu, G. J. Cheng, W. Hu, *Nat. Commun.* **2020**, *11*, 2308.
- [32] J. Yan, H. Pang, L. Xu, J. Yang, R. Quhe, X. Zhang, Y. Pan, B. Shi, S. Liu, L. Xu, J. Yang, F. Pan, Z. Zhang, J. Lu, *Adv. Electron. Mater.* **2019**, *5*, 1900226.
- [33] G. Qiu, C. Niu, Y. Wang, M. Si, Z. Zhang, W. Wu, P. D. Ye, *Nat. Nanotechnol.* **2020**, *15*, 585.
- [34] G. Rao, X. Wang, Y. Wang, P. Wangyang, C. Yan, J. Chu, L. Xue, C. Gong, J. Huang, J. Xiong, Y. Li, *InfoMat* **2019**, *1*, 272.
- [35] X. Cai, Y. Ren, M. Wu, D. Xu, X. Luo, *Nanoscale* **2020**, *12*, 167.
- [36] Y. Wang, C. Xiao, M. Chen, C. Hua, J. Zou, C. Wu, J. Jiang, S. A. Yang, Y. Lu, W. Ji, *Mater. Horiz.* **2018**, *5*, 521.
- [37] Q. Zhang, S. Zuo, P. Chen, C. Pan, *InfoMat* **2021**, *3*, 987.
- [38] R. G. Musket, *Surf. Sci.* **1978**, *74*, 423.
- [39] A. S. Pine, G. Dresselhaus, *Phys. Rev. B* **1971**, *4*, 356.
- [40] S. Yang, Y. Chen, C. Jiang, *InfoMat* **2021**, *3*, 397.
- [41] R. Beams, L. G. Cançado, S. Krylyuk, I. Kalish, B. Kalanyan, A. K. Singh, K. Choudhary, A. Bruma, P. M. Vora, F. Tavazza, A. V. Davydov, S. J. Stranick, *ACS Nano* **2016**, *10*, 9626.
- [42] L. Zhao, C. A. Belvin, R. Liang, D. A. Bonn, W. N. Hardy, N. P. Armitage, D. Hsieh, *Nat. Phys.* **2017**, *13*, 250.
- [43] Z. Sun, Y. Yi, T. Song, G. Clark, B. Huang, Y. Shan, S. Wu, D. Huang, C. Gao, Z. Chen, M. McGuire, T. Cao, D. Xiao, W.-T. Liu, W. Yao, X. Xu, S. Wu, *Nature* **2019**, *572*, 497.
- [44] J. Chu, Y. Wang, X. Wang, K. Hu, G. Rao, C. Gong, C. Wu, H. Hong, X. Wang, K. Liu, C. Gao, J. Xiong, *Adv. Mater.* **2021**, *33*, 2004469.
- [45] L. Cai, Y. Tian, X. Yuan, G. Hu, J. Ren, *Appl. Surf. Sci.* **2016**, *389*, 916.
- [46] M. N. Blonsky, H. L. Zhuang, A. K. Singh, R. G. Hennig, *ACS Nano* **2015**, *9*, 9885.
- [47] L. Dong, J. Lou, V. B. Shenoy, *ACS Nano* **2017**, *11*, 8242.
- [48] K.-A. N. Duerloo, M. T. Ong, E. J. Reed, *J. Phys. Chem. Lett.* **2012**, *3*, 2871.
- [49] M. M. Alyörük, Y. Aierken, D. Çakır, F. M. Peeters, C. Sevik, *J. Phys. Chem. C* **2015**, *119*, 23231.
- [50] R. Talley Kevin, L. Perkins Craig, R. Diercks David, L. Brennecke Geoff, A. Zakutayev, *Science* **2021**, *374*, 1488.
- [51] N. Balke, P. Maksymovych, S. Jesse, A. Herklotz, A. Tselev, C.-B. Eom, I. I. Kravchenko, P. Yu, S. V. Kalinin, *ACS Nano* **2015**, *9*, 6484.
- [52] S. S. Cheema, D. Kwon, N. Shanker, R. dos Reis, S.-L. Hsu, J. Xiao, H. Zhang, R. Wagner, A. Datar, M. R. McCarter, C. R. Serrao, A. K. Yadav, G. Karbasian, C.-H. Hsu, A. J. Tan, L.-C. Wang, V. Thakare, X. Zhang, A. Mehta, E. Karapetrova, R. V. Chopdekar, P. Shafer, E. Arenholz, C. Hu, R. Proksch, R. Ramesh, J. Ciston, S. Salahuddin, *Nature* **2020**, *580*, 478.
- [53] R. K. Vasudevan, N. Balke, P. Maksymovych, S. Jesse, S. V. Kalinin, *Appl. Phys. Rev.* **2017**, *4*, 021302.
- [54] N. Higashitarumizu, H. Kawamoto, C.-J. Lee, B.-H. Lin, F.-H. Chu, I. Yonemori, T. Nishimura, K. Wakabayashi, W.-H. Chang, K. Nagashio, *Nat. Commun.* **2020**, *11*, 2428.
- [55] Y. Pan, S. Li, M. Ye, R. Quhe, Z. Song, Y. Wang, J. Zheng, F. Pan, W. Guo, J. Yang, J. Lu, *J. Phys. Chem. C* **2016**, *120*, 13063.
- [56] M. Si, A. K. Saha, S. Gao, G. Qiu, J. Qin, Y. Duan, J. Jian, C. Niu, H. Wang, W. Wu, S. K. Gupta, P. D. Ye, *Nat. Electron.* **2019**, *2*, 580.
- [57] C. C. Neacsu, B. B. van Aken, M. Fiebig, M. B. Raschke, *Phys. Rev. B* **2009**, *79*, 100107.
- [58] X. Zhang, X.-F. Qiao, W. Shi, J.-B. Wu, D.-S. Jiang, P.-H. Tan, *Chem. Soc. Rev.* **2015**, *44*, 2757.
- [59] J. Xiao, H. Zhu, Y. Wang, W. Feng, Y. Hu, A. Dasgupta, Y. Han, Y. Wang, D. A. Muller, L. W. Martin, P. Hu, X. Zhang, *Phys. Rev. Lett.* **2018**, *120*, 227601.